# Low-lying $E1$ strength in $^{20}$O

E. Tryggestad,* T. Baumann, P. Heckman, and M. Thoennessen
*National Superconducting Cyclotron Laboratory, Michigan State University, East Lansing, Michigan 48824, USA and Michigan State University, Department of Physics and Astronomy, East Lansing, Michigan 48824, USA*

T. Aumann,† D. Bazin, and Y. Blumenfeld‡
*National Superconducting Cyclotron Laboratory, Michigan State University, East Lansing, Michigan 48824, USA*

J. R. Beene, T. A. Lewis, D. C. Radford, D. Shapira, and R. L. Varner
*Physics Division, Oak Ridge National Laboratory, Oak Ridge, Tennessee 37831, USA*

M. Chartier§
*National Superconducting Cyclotron Laboratory, Michigan State University, East Lansing, Michigan 48824, USA and Physics Division, Oak Ridge National Laboratory, Oak Ridge, Tennessee 37831*

M. L. Halbert
*University of Tennessee, Department of Physics and Astronomy, Knoxville, Tennessee 37996, USA*

J. F. Liang
*Oak Ridge Associated Universities, Oak Ridge, Tennessee 37831, USA*

(Received 27 February 2003; published 23 June 2003)

Intermediate energy Coulomb excitation at 100 MeV/nucleon was used to probe the low-lying level structure of both $^{18}$O and $^{20}$O in the region between 1 and 8 MeV. Discrete $1^-$ states with energies of 5.35(10) and 6.85(5) MeV were observed in $^{20}$O. The strong direct excitation and subsequent $\gamma$-ray decay of these states, along with $B(E\lambda)$ predictions for $^{18,20}$O levels in this energy region, established their dipole character. The extracted $B(E1)\uparrow$ values of $0.062(16)e^2$ fm$^2$ and $0.035(9)e^2$ fm$^2$ for the 5.35- and 6.85-MeV states, respectively, are significantly larger than shell model calculations, though modification of the single-particle energies, in particular, the $p$-$sd$ shell gap, improves the agreement. The summed $B(E1)\uparrow$ value for these levels (in Weisskopf units) is consistent with that for other nuclei that have been discussed recently in the literature as potential Pygmy dipole resonance hosts.

DOI: 10.1103/PhysRevC.67.064309 PACS number(s): 25.70.De, 25.20.Dc, 24.30.Gd, 24.10.Lx

## I. INTRODUCTION

Collective modes are nuclear excitations that can be described within the context of cooperative motion of the individual nucleons. They are important probes of nuclear structure. The isovector giant dipole resonance (IVGDR) is arguably the most accessible of the collective modes, and therefore has been studied rather extensively in the stable nuclei. In heavy, spherical nuclei, the average excitation energy of this single-peaked resonance, $E_{\mathrm{GDR}}$, varies rather smoothly with the number of nucleons (as $A^{-1/3}$). In lighter nuclei, $A \leqslant 50$, the IVGDR energies are seen to deviate from this simple relation, favoring lower values. Additionally, the IVGDR excitation (or strength) function for lighter systems tends to display multiple peaks, which is the signature of the individual nucleon (or single-particle) structure. Such effects are indicative of the breakdown of the simple macroscopic description of the giant resonance.

The recent availability of radioactive beams has offered the possibility to explore exotic nuclei that are proton-neutron asymmetric. Indeed, the different shell structure in these nuclei affects the dynamics of collective excitations. For example, moving towards neutron instability the excitation function for the IVGDR mode is expected to fragment substantially, giving rise to a strength increase at lower excitation energies (e.g., Refs. [1,2]).

Over the last decade, significant experimental and theoretical effort has been dedicated to the question of the nature of low-lying $E1$ strength in neutron-rich nuclei: in particular, whether or not these dipole excitations can be attributed to collectivity. In the lightest of neutron-rich nuclei, the so-called halo systems such as $^{6,8}$He, $^{11}$Li, and $^{11}$Be, enhancements in the dipole strength functions have been observed (e.g., see Refs. [3–6]). For example, in $^{11}$Be the summed $B(E1)$ strength between 0 and 4.5 MeV of excitation energy is 4.0(9) W.u. [6]. Indeed, comparison of this value with that for typical discrete states in stable nuclei of $10^{-3}$ W.u. re-

*Present address: Institut de Physique Nucléaire, $IN_2P_3$-CNRS, 91406 Orsay Cedex, France. Email address: tryggest@ipno.in2p3.fr
†Present address: Gesellschaft für Schwerionenforschung, Planckstrasse 1, 64291 Darmstadt, Germany
‡Present address: Institut de Physique Nucléaire, $IN_2P_3$-CNRS, 91406 Orsay Cedex, France.
§Present address: University of Liverpool, Department of Physics, Oliver Lodge Laboratory, Oxford Street, Liverpool L69 7ZE, United Kingdom.

 ©2003 The American Physical Society

veals this enhancement to be quite extraordinary. The shape of the observed $E1$ excitation functions in these halo nuclei—specifically the systematic appearance of a broad peak at an excitation energy of approximately 1 MeV (near the breakup threshold)—seemed to suggest a collective soft dipole resonance, wherein the halo neutrons oscillate out of phase with the residual nuclear core, might be the mechanism.

The analogous collective scenario in heavier neutron-rich nuclei—the Pygmy dipole resonance (PDR)—is proposed as an oscillation of the neutrons comprising the neutron skin (valence neutrons) against the remaining, tightly-bound core. Because this resonance relies on the existence of the neutron skin, its evolution with neutron excess for a given isotopic chain is expected to be rather smooth. Low-lying dipole strength observed near or below the neutron separation threshold in stable nuclei such as $^{48}$Ca, $^{116,124}$Sn, $^{138,140}$Ba, $^{140}$Ce, and $^{204,206,208}$Pb has been discussed in this context [7–11].

Given the wealth of theoretical models, ranging from macroscopic (e.g., the three fluid model of nuclei [12]) to microscopic (e.g., the quasiparticle-phonon model—QPM [8,13], the density functional theory—DFT [14], or the random phase approximation—RPA [15]), that have been used for comparison with the experimental results, in some cases conflicting interpretations have been offered as to the underlying mechanism for this low-lying dipole strength. For example, the magnitude of low-lying $E1$ strength observed in $^{48}$Ca following a $^{40,48}$Ca nuclear resonance fluorescence study at the S-DALINAC facility [7] is in good agreement with phonon damping model (PDM) calculations; within this framework the associated states are derived from noncollective $p$-$h$ excitations that gain strength from the GDR (see, e.g., Ref. [16]). Yet, The PDM overpredicts the strength observed in $^{40}$Ca. A collective skin resonance predicted within the DFT for $^{48}$Ca [14] agrees well with experiment as far as the energy of the resonance is concerned, but overpredicts the observed strength for the concentration of dipole states.

Also noteworthy for this discussion are the results from an S-DALINAC study of the $^{204,206,208}$Pb isotopes [11], which revealed two clusters of $E1$ strength at $\sim$5 and $\sim$6 MeV in each isotope. QPM calculations do reproduce well, for example, the trend regarding increasing fragmentation of dipole strength going from $^{208}$Pb to $^{204}$Pb (which is attributable to the opening of the neutron shell). However, the centroids of the observed clusters are systematically overpredicted. The strength for these clusters of low-lying states in the QPM is dominated by constructive interference of the one- and two-phonon configurations (as a similar comparison for $^{116,124}$Sn, $^{138}$Ba, and $^{140}$Ce reveals [8–10]). This effect cannot be ascribed to collectivity in any obvious way. For the case of $^{208}$Pb, a set of RPA calculations that predict two coherent $p$-$h$ resonances near 9 MeV [15] are perhaps contrary to the QPM results.

It is rather apparent that there exists a significant need for experimental data, especially for more complete evolutionary studies along isotopic chains. Such systematic information will better constrain theoretical models, perhaps revealing those that are better suited for application to this important question.

### A. Motivation

The heavier oxygen isotopes, pictured as a doubly magic $^{16}$O core surrounded by a valence neutron skin, are ideal candidates for such an evolutionary PDR study. Indeed, indications of a trend for increasing low-energy dipole strength with mass can be observed in the dipole excitation functions (above threshold) for the stable oxygen isotopes [17,18]. One would like to extend this comparison towards the neutron drip line, focusing on the more interesting short-lived isotopes. The LAND (Large Area Neutron Detector) Collaboration at GSI was able to elucidate the GDR strength functions of the oxygen isotopes $^{17-22}$O by measuring the photoneutron cross sections. Their results were generally consistent with the theoretical prediction regarding the shifting of dipole strength to lower energies [19]. However, the extent to which collectivity plays a role at low energies remains to be demonstrated.

Measurement of $E1$ strength in radioactive nuclei generally relies on Coulomb excitation of a short-lived projectile. The excitation of bound states can then be studied via the subsequent $\gamma$ decays. Above the particle threshold, the best technique involves detection of the evaporated particles. This method, utilized by the LAND Collaboration, is also referred to as virtual photon absorption. In principle, it is also possible to detect the $\gamma$-ray decay above the particle thresholds, though the $\gamma$-ray emission probability is significantly reduced compared to the neutron evaporation. Hence, for GDR-region studies such an approach demands comparatively higher radioactive beam intensities and/or energies. Nevertheless, this virtual photon scattering method has been applied successfully in a measurement of the $^{11}$Be $E1$ strength function between 9 and 25 MeV (above $S_{2n}$) [20].

Low-lying discrete states in $^{20}$O have been probed mainly via transfer reactions with stable beams [21]. More recently, radioactive-beam studies have investigated the structure of $^{20}$O by exciting the $2^+_{1,2}$ and $3^-_1$ states [22,23] and $^{22}$O by exciting the $2^+_1$ state [24]. However, no bound $1^-$ states have been identified in $^{20}$O. The present study used Coulomb excitation of a radioactive beam to search for $E1$ strength in $^{20}$O. To facilitate a straightforward comparison of our result with a known case, we also performed a measurement with stable $^{18}$O. In the remainder of this paper we will discuss, in detail, the analysis leading to the results extracted from our measurements. We would like to note that a summary of this work can also be found in Ref. [25].

### B. Review of Coulomb excitation

Coulomb excitation is a well-understood process that occurs as a result of electromagnetic interactions of a projectile ($Z_A$) with a target ($Z_B$). One of the participating nuclei is excited as it passes through the electromagnetic field of the other. The process can be described as the absorption of a virtual photon by either the target or the projectile. Because in pure Coulomb excitation the participating nuclei stay outside the range of the nuclear strong force, the excitation cross

TABLE I. Relevant low-lying level structure of $^{18}$O with known $B(\pi\lambda)$ information [28–30]. For all of these states the $\gamma$-ray decay branching ratios are known [31]. The values in square brackets indicate powers of 10.

| $(e,e')$ scattering on $^{18}$O | | |
|---|---|---|
| $E_x$ (MeV) | $J_n^\pi$ | $B(\pi\lambda)\uparrow$ ($e^2$ fm$^{2\lambda}$) |
| 1.98 | $2_1^+$ | 4.48(13) [+01] [a] |
| 3.92 | $2_2^+$ | 2.22(10) [+01] [a] |
| 4.46 | $1_1^-$ | $<$4 [-06] [b] |
| 5.10 | $3_1^-$ | 1.301(39) [+03] [b] |
| 5.26 | $2_3^+$ | 2.83(15) [+01] [a] |
| 5.53 | $2_1^-$ | $<$1.9 [-03] [c] |
| 6.20 | $1_2^-$ | 2.19(36) [-03] [b] |
| 6.35 | $2_2^-$ | $<$2.0 [-03] [c] |
| 6.40 | $3_2^-$ | 4.0(9) [+01] [b] |
| 7.62 | $1_3^-$ | 6.1(13) [-04] [b] |
| 7.77 | $2_3^-$ | 9.0(32) [-02] [c] |

[a]Reference [28].
[b]Reference [29].
[c]Reference [30].

section can be expressed in terms of the same multipole matrix elements that characterize excited-state $\gamma$-ray decay, or the reduced transition probabilities, $B(\pi\lambda;I_i\rightarrow I_f)$. Hence, Coulomb excitation amplitudes are strongly coupled with valuable nuclear structure information.

This fact becomes evident upon closer examination of expressions for the differential Coulomb cross section for a projectile nucleus that has been taken from state $|i\rangle$ to state $|f\rangle$ following the absorption of a virtual photon (e.g., Ref. [26]):

$$\frac{d\sigma_{E\lambda}}{d\Omega}=\left(\frac{Z_{\mathrm{B}}e}{\hbar v}\right)^2 a^{-2\lambda+2}B(E\lambda;I_i\rightarrow I_f)\frac{df_{E\lambda}(\vartheta,\xi)}{d\Omega},$$

$$\frac{d\sigma_{M\lambda}}{d\Omega}=\left(\frac{Z_{\mathrm{B}}e}{\hbar c}\right)^2 a^{-2\lambda+2}B(M\lambda;I_i\rightarrow I_f)\frac{df_{M\lambda}(\vartheta,\xi)}{d\Omega}, \quad (1)$$

where $a$ is half the distance of closest approach, $\xi$ is the adiabaticity parameter, $v$ is the incoming velocity of the projectile, and $\vartheta$ is the scattering angle of the projectile in the center of mass. $df_{\pi\lambda}/d\Omega$ are the differential cross section functions that are defined in Refs. [26,27]. The reduced transition probability itself is proportional to the multipole matrix element. Specifically,

$$B(\pi\lambda;I_i\rightarrow I_f)=\frac{1}{2I_i+1}|\langle I_f\|\mathcal{M}(\pi\lambda)\|I_i\rangle|^2. \quad (2)$$

This matrix element depends directly on the overlap of the wave functions of the involved states, $|I_i\rangle$ and $|I_f\rangle$, and, therefore can be thought of as a gauge for collectivity in the nuclear transition, i.e, Coulomb excitation tends to probe collective features in nuclei such as rotation, vibration, or deformation.

It should be noted that the derivation of Eq. (1) involves a semiclassical approach. Herein, the trajectory of the projectile is treated classically, assuming a Rutherford scattering distribution, while the interaction that causes the nuclear transition in the projectile or target is found using first-order perturbation theory, i.e.,

$$\frac{d\sigma}{d\Omega}=\left(\frac{d\sigma}{d\Omega}\right)_{\mathrm{Ruth}}P_{i\rightarrow f}, \quad (3)$$

where the probability $P_{i\rightarrow f}$ is given by the square of amplitude of the nuclear excitation process, $a_{i\rightarrow f}$:

$$a_{i\rightarrow f}=\frac{1}{i\hbar}\int_{-\infty}^{\infty}\langle f|V[\mathbf{r}(t)]|i\rangle e^{i(E_f-E_i)/\hbar}dt. \quad (4)$$

The explicit form of the potential $V[\mathbf{r}(t)]$, of course, depends on whether the excitations are electric or magnetic.

### C. Low-lying level structure of $^{18}$O and $^{20}$O

Table I shows the pertinent level structure of $^{18}$O, incorporating all states below the neutron separation energy ($S_n=8.044$ MeV) which are accessible by Coulomb excitation. Given this level scheme the $^{18}$O analysis considered $E1$, $E2$, $E3$, and $M2$ virtual excitations. Substitution of the differential cross section functions into the expressions presented above [Eq. (1)] leads to

$$\frac{d\sigma_{E1}(\vartheta,\xi)}{d\Omega}=\frac{\pi}{18}\left(\frac{Z_{\mathrm{B}}\alpha}{\beta}\right)^2\frac{B(E1;I_i\rightarrow I_f)}{\sin^4\left(\frac{\vartheta}{2}\right)}\times[I_{1-1}^2(\vartheta,\xi)+I_{11}^2(\vartheta,\xi)],$$

$$\frac{d\sigma_{E2}(\vartheta,\xi)}{d\Omega}=\frac{\pi}{25}\left(\frac{Z_{\mathrm{B}}\alpha}{\beta}\right)^2\frac{B(E2;I_i\rightarrow I_f)}{a^2\sin^4\left(\frac{\vartheta}{2}\right)}\times\left[\left(\frac{3}{8}\right)\{I_{2-2}^2(\vartheta,\xi)+I_{22}^2(\vartheta,\xi)\}+\left(\frac{1}{4}\right)I_{20}^2(\vartheta,\xi)\right],$$

$$\frac{d\sigma_{E3}(\vartheta,\xi)}{d\Omega}=\frac{\pi}{49}\left(\frac{Z_{\mathrm{B}}\alpha}{\beta}\right)^2\frac{B(E3;I_i\rightarrow I_f)}{a^4\sin^4\left(\frac{\vartheta}{2}\right)}\times\left[\left(\frac{5}{16}\right)\{I_{3-3}^2(\vartheta,\xi)+I_{33}^2(\vartheta,\xi)\}+\left(\frac{3}{16}\right)\{I_{3-1}^2(\vartheta,\xi)+I_{31}^2(\vartheta,\xi)\}\right],$$

$$\frac{d\sigma_{M2}(\vartheta,\xi)}{d\Omega}=\frac{\pi}{25}(Z_{\mathrm{B}}\alpha)^2\frac{B(M2;I_i\rightarrow I_f)\cot^2\left(\frac{\vartheta}{2}\right)}{a^2\sin^4\left(\frac{\vartheta}{2}\right)}$$

$$\times\left[\left(\frac{3}{32}\right)\{I^2_{3-1}(\vartheta,\xi)+I^2_{31}(\vartheta,\xi)\}\right], \quad (5)$$

where $\beta$ is the incoming velocity of the projectile and $\alpha=e^2/\hbar c$. It is thus assumed that the reduced transition probability is expressed in units of $e^2\,\mathrm{fm}^{2\lambda}$. The $I_{\lambda\mu}(\vartheta,\xi)$ functions in Eq. (5) are defined in Refs. [26,27] as the Coulomb excitation functions, where they can be found in complicated integral form. The fact that the projectiles detected in this study were limited to small forward angles, however, ensures that an approximate expression for the $I_{\lambda\mu}(\vartheta,\xi)$ functions,

$$I_{\lambda\mu}(\vartheta,\xi)\simeq\frac{(-1)^{(\lambda-\mu)/2}}{\varepsilon}\left(\frac{\xi}{2\varepsilon}\right)^{(\lambda-1)/2}\Gamma\left(\frac{-\lambda+\mu+1}{2}\right)$$

$$\times e^{-\pi\xi/2}W_{-\mu/2-\lambda/2}(2\xi\varepsilon), \quad (6)$$

is adequate. The $W_{-\mu/2-\lambda/2}(2\xi\varepsilon)$ quantities in Eq. (6) are Whittaker functions, which are related to confluent hypergeometric functions, $U(a,c;z)$ [32]. Specifically,

$$W_{lm}(x)=e^{-x/2}x^{m+1/2}U(m-l+1/2,2m+1;x). \quad (7)$$

Making use of the above formalism, preliminary cross-section calculations were performed to gain perspective regarding the relative importance of the possible excitation channels for $^{18}$O. The results of these calculations, presented in Table II, clearly reveal that quadrupole strength will dominate the $^{18}$O discrete-region excitation function. The analysis and interpretation of the results for these studies must also incorporate the possibility for target excitation. Table II also states the results of calculations for the first-excited $2^+$ and $3^-$ levels in the target which have $B(E\lambda)\uparrow$ strengths of $2.9(3)\times10^3e^2\,\mathrm{fm}^4$ and $6.11(9)\times10^5e^2\,\mathrm{fm}^6$, respectively [33,34]. [To convert the expressions of Eq. (5) to relations that are valid for target excitation, one needs only to exchange $Z_{\mathrm{B}}$ for $Z_{\mathrm{A}}$.] The calculations suggest that excitation of its $2^+_1$ configuration, for example, will account for approximately 20% of the total $^{18}$O+$^{208}$Pb quadrupole strength, which is significant.

Based on the Coulomb excitation cross section calculations for $^{18}$O, it is indeed reasonable to assume that an analysis that includes only electric virtual excitations, namely, $E1$, $E2$, and $E3$, will be adequate for the $^{20}$O study. The left panel of Table III summarizes the pertinent status of $^{20}$O spectroscopy [21]. Aside from our knowledge of the $B(E2)$ for the $2^+$ at 1.67 MeV and the branching from the $2^+$ at 4.07 MeV, only the energies (and in most cases the spin parity) of observed $^{20}$O levels have been established. Notice that apart from the tentative $3^-$ assignment of the 5.61-MeV state, no experimental information regarding the $^{20}$O negative parity, discrete structure exists.

A theoretical analysis of the low-lying $^{20}$O structure is presented in the right panel of Table III. This is a summary

TABLE II. The result of total Coulomb excitation cross section calculations for excitations to low-lying $1^-$, $2^+$, $3^-$, and $2^-$ states in $^{18}$O and $^{208}$Pb assuming an energy of 100 MeV/nucleon for incident $^{18}$O projectiles and a center-of-mass angular acceptance of 20 mrad for scattered projectiles. The projectile $B(\pi\lambda)$ information was taken from electron-scattering studies [28–30], while that for the target was taken from Refs. [33,35]. The values in square brackets indicate powers of 10.

| $J^\pi_n$ | $E_x$ (MeV) | $B(\pi\lambda)\uparrow(e^2\,\mathrm{fm}^{2\lambda})$ | $\sigma$ ($\mu$b) |
|---|---|---|---|
| | | Projectile ($^{18}$O) | |
| $1^-_1$ | 4.46 | $<4$ [-06] | $<3$ [-01] |
| $1^-_2$ | 6.20 | 2.19 [-03] | 4.80 [+01] |
| $1^-_3$ | 7.62 | 6.1 [-04] | 5.2 [+00] |
| $2^+_1$ | 1.98 | 4.48 [+01] | 2.27 [+03] |
| $2^+_2$ | 3.92 | 2.22 [+01] | 7.66 [+02] |
| $2^+_3$ | 5.26 | 2.83 [+01] | 6.41 [+02] |
| $3^-_1$ | 5.10 | 1.301 [+03] | 1.145 [+01] |
| $3^-_1$ | 6.40 | 4.0 [+01] | 3.0 [-01] |
| $2^-_1$ | 5.53 | $<1.9$ [-03] | $<3.2$ [-03] |
| $2^-_2$ | 6.35 | $<2.0$ [-03] | $<2.3$ [-03] |
| $2^-_3$ | 7.77 | 9.0 [-02] | 5.5 [-02] |
| | | Target ($^{208}$Pb) | |
| $2^+_1$ | 4.09 | 2.9 [+03] | 9.1 [+02] |
| $3^-_1$ | 2.61 | 6.11 [+05] | 5.30 [+01] |

that combines results from $1s0d$-USD and $0s0p$–$1s0d$–$1p0f$-WBP shell model calculations for lowest-lying positive- ($J=2$) and negative-parity ($J=1,3$) levels, respectively [36–38]. Comparing the $B(E2)\uparrow$ predictions for $^{20}$O with measured $B(E2)\uparrow$ strengths for the low-lying $2^+$ states in $^{18}$O (see Table I), we expect *a priori* a

TABLE III. Left panel: The current $^{20}$O experimental level scheme for $J<4$ states below the neutron binding energy ($S_n=7.608$ MeV). The $\gamma$-ray decay branching is known only for the $2^+$ state at 4.07 MeV [21]. Right panel: The pertinent $^{20}$O theoretical level structure as calculated by Brown [36]. The positive parity states have been calculated using the $1s0d$-USD interaction [37], while the negative parity results have made use of the $0s0p$–$1s0d$–$1p0f$-WBP interaction [38]. The values in square brackets indicate powers of 10.

| $^{20}$O known level scheme | | | $^{20}$O theory (USD/WBP) | | |
|---|---|---|---|---|---|
| $E_x$ (MeV) | $J^\pi$ | $B(E\lambda)\uparrow$ [a] | $E_x$ (MeV) | $J^\pi_n$ | $B(E\lambda)\uparrow$ [a] |
| 1.67 | $2^+$ | 2.8(2) [+01] | 2.0 | $2^+_1$ | 2.9 [+01] |
| 4.07 | $2^+$ | | 4.2 | $2^+_2$ | 7.8 [+00] |
| 5.00 | | | 5.0 | $3^-_1$ | 1.6 [+03] |
| 5.23 | $2^+$ | | 5.1 | $1^-_1$ | 2.4 [-03] |
| 5.30 | $2^+$ | | 5.3 | $2^+_3$ | 7.0 [-04] |
| 5.61 | $(3^-)$ | | 5.5 | $3^-_2$ | 7.0 [+02] |
| 6.55 | (2) | | 6.2 | $1^-_2$ | 1.7 [-03] |
| | | | 7.2 | $1^-_3$ | 1.4 [-03] |
| | | | 7.7 | $1^-_4$ | 4.1 [-02] |
| | | | 8.0 | $2^+_4$ | 6.6 [-01] |

[a] $[B(E\lambda)]=e^2\,\mathrm{fm}^{2\lambda}$.

TABLE IV. The structure of the calculated $^{20}$O $1^-$ states in Table III. The partition is given for those configurations that give a contribution of at least 8% to the total wave function.

| $E_x$ (MeV) | Configuration | Wave function contribution (%) |
|---|---|---|
| 5.1 | $(0p_{1/2})^{-1}(0d_{5/2})^4(1s_{1/2})^1$ | 27.48 |
| | $(0p_{1/2})^{-1}(0d_{5/2})^5$ | 10.71 |
| | $(0p_{1/2})^{-1}(0d_{5/2})^3(0d_{3/2})^1(1s_{1/2})^1$ | 8.80 |
| | $(0p_{1/2})^{-1}(0d_{5/2})^2(1s_{1/2})^3$ | 8.47 |
| 6.2 | $(0p_{1/2})^{-1}(0d_{5/2})^4(1s_{1/2})^1$ | 56.92 |
| | $(0p_{3/2})^{-1}(0d_{5/2})^4(1s_{1/2})^1$ | 10.46 |
| 7.2 | $(0p_{1/2})^{-1}(0d_{5/2})^4(1s_{1/2})^1$ | 41.59 |
| | $(0p_{1/2})^{-1}(0d_{5/2})^3(1s_{1/2})^2$ | 12.39 |
| 7.7 | $(0p_{1/2})^{-1}(0d_{5/2})^4(1s_{1/2})^1$ | 24.09 |
| | $(0p_{1/2})^{-1}(0d_{5/2})^5$ | 16.57 |
| | $(0p_{3/2})^{-1}(0d_{5/2})^5$ | 8.45 |

marked relative suppression of $E2$ strength in the radioactive beam study. This is a manifestation of the fact that the two-particle $(2p)$ $(1s0d)^2$ configurations in $^{18}$O are mixed strongly with intruder $4p$-$2h$ $(0p)^{-2}(1s0d)^4$ configurations (e.g., Ref. [39]), whereas the low-lying $2^+$ states in $^{20}$O comprise mostly $4p$ $(1s0d)^4$ excitations (since the intruder configurations are thought to exist at higher excitation energies) [36]. Contrasting this is the trend that unfolds from a comparison of the $^{20}$O $B(E1)\uparrow$ predictions with the measured $^{18}$O values for the lowest $1^-$ states. A relative increase in low-lying dipole strength in the neutron-richer $^{20}$O is expected. The structure of the calculated $1^-$ states in $^{20}$O is provided in Table IV, where the partitioning is shown for those configurations that give a contribution of at least 8% to the total wave function [36].

Table V shows the results for the Coulomb excitation cross section calculations for the $^{20}$O+ $^{208}$Pb system, based on the theoretical spectrum listed in Table III. It demonstrates the predicted strong population of $1^-$ states in contrast to the stable $^{18}$O system (see Table II).

## II. EXPERIMENT AND DATA ANALYSIS

The experiments were carried out at the National Superconducting Cyclotron Laboratory (NSCL) at Michigan State University. For the first study, $^{18}$O was accelerated in the K1200 superconducting cyclotron to an energy of 100 MeV/nucleon and delivered directly to the target. For the radioactive beam experiment, a primary beam of $^{22}$Ne was first accelerated in the K1200 to an energy of 120 MeV/nucleon. This beam impinged on a thick $^{9}$Be production target. Fragments produced via projectile fragmentation were then analyzed with the A1200 fragment separator [40]. Using its combination of two magnetic bends along with a wedge-shaped energy degrader and momentum slits, this device was adjusted to select 100 MeV/nucleon $^{20}$O with a momentum spread $(\Delta p/p)$ of $\pm 0.5\%$ and a purity of approximately 85%.

TABLE V. Coulomb excitation cross section calculations for the $^{20}$O+ $^{208}$Pb system assuming an energy of 100 MeV/nucleon for incident $^{20}$O projectiles and a center-of-mass angular acceptance of 20 mrad for scattered projectiles. The theoretical $B(E\lambda)$ are taken from Table III. The values in square brackets indicate powers of 10.

| | Projectile ($^{20}$O) | | |
|---|---|---|---|
| $J_n^\pi$ | $E_x^{\rm th}$ (MeV) | $B(E\lambda)^{\rm th}\uparrow(e^2\,{\rm fm}^{2\lambda})$ | $\sigma^{\rm th}$ ($\mu$b) |
| $1_1^-$ | 5.1 | 2.4 [-03] | 1.7 [+02] |
| $1_2^-$ | 6.2 | 1.7 [-03] | 6.3 [+01] |
| $1_3^-$ | 7.2 | 1.4 [-03] | 3.0 [+01] |
| $1_4^-$ | 7.7 | 4.1 [-02] | 6.5 [+02] |
| $2_1^+$ | 2.0 | 2.9 [+01] | 1.9 [+03] |
| $2_2^+$ | 4.2 | 7.8 [+00] | 3.7 [+02] |
| $2_3^+$ | 5.3 | 7.0 [-04] | 2.5 [-02] |
| $2_4^+$ | 8.0 | 6.6 [-01] | 1.0 [+01] |
| $3_1^-$ | 5.0 | 1.6 [+03] | 2.4 [+01] |
| $3_1^-$ | 5.5 | 7.0 [+02] | 1.0 [+01] |
| | Target ($^{208}$Pb) | | |
| $2_1^+$ | 4.09 | 2.9 [+03] | 1.3 [+03] |
| $3_1^-$ | 2.61 | 6.11 [+05] | 8.49 [+01] |

The $^{18,20}$O projectiles impinged on a 30 mg/cm$^2$ enriched (99.09%) $^{208}$Pb target. Resulting reaction products were analyzed using the S800 spectrograph (e.g., Ref. [41]) which was placed at 0° with respect to the beam axis. The available intensity of the $^{18}$O beam (approximately $2.5\times10^9$ particles/s) was experimentally limited by the capabilities of the S800 focal plane detectors [42], which can count up to (approximately) $10^4$ reaction products per second. The $^{20}$O intensity from the secondary-beam process was $5\times10^5$ particles/s. The S800 focal plane detection arrangement [42] allowed for unambiguous fragment identification (in both $Z$ and $A$). The kinetic energies of identified $^{18,20}$O fragments were calculated from position and trajectory information at the focus using the ion optics code COSY INFINITY. An energy resolution of approximately 1 part in 7000 $(1\sigma)$ for both experiments was achieved carrying these COSY reconstruction calculations to second order.

Decay $\gamma$ rays in coincidence with reaction fragments were detected using the large ORNL-TAMU-MSU $BaF_2$ array [43,44] (144 individual elements in the present configuration), which was positioned 45-cm downstream from the target and tightly packed around the beam pipe in a concentric arrangement. A depiction of the front face of the $BaF_2$ array is shown in Fig. 1. The $\gamma$-ray events were identified using both time of flight (TOF) and pulse-height constraints to suppress the background consisting mostly of neutrons that were detected in coincidence with an uncorrelated fragment. Examples of this process are shown in Fig. 2 for a sample of $^{18}$O-$BaF_2$ coincidence events. In Fig. 2(a), a gate is placed on a two-dimensional (2D) histogram which displays calibrated $BaF_2$ energy for individual detector hits against the time of flight parameter. Specifically, this TOF parameter is a measure of the time between the cyclotron rf logic signal and the logic pulse from an individual $BaF_2$ detector. In this figure the prompt $\gamma$ rays appear as a pronounced vertical band.

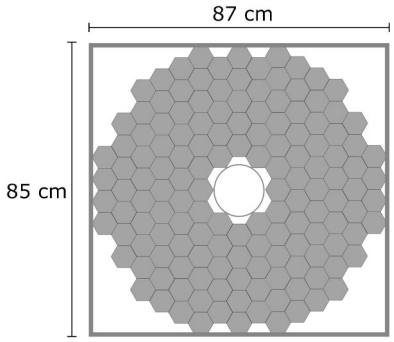


FIG. 1. The front face of the $BaF_2$ array which consisted of 144 individual hexagonal crystals. The center of the array coincided with the beam axis.

These events are superimposed with a periodic structure that is a distinctive feature of the uncorrelated or random background. (The periodicity of this random background, of course, mirrors that of the cyclotron rf.)

Figure 2(b) demonstrates the pulse shape discrimination capability of $BaF_2$ detectors [45,46]. Neutrons can be separated from $\gamma$ rays for individual detector events of $\gtrsim 8$ MeV.

The settings of the $BaF_2$ array for both the $^{18}O$ and the $^{20}O$ study were identical with the exception of an adjustment made to the $BaF_2$ energy thresholds—the thresholds were lowered for the case of $^{20}O$ because the background counting rate was reduced, given the significantly lower secondary-beam intensity. More discussion pertaining to the threshold settings will follow in Sec. III A.

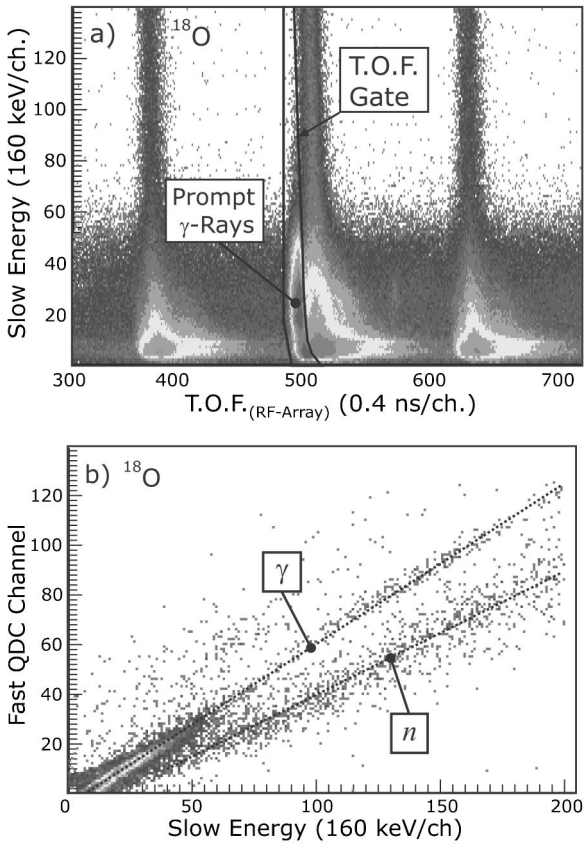


FIG. 2. (a) $BaF_2$ energy vs TOF for $^{18}O$ coincidence events showing the prompt $\gamma$-ray gate used to select the individual detector hits of interest. (b) A fast vs slow 2D histogram generated from hits in a particular detector with $^{18}O$ coincidence data. Above $\sim 8$ MeV, neutrons appear below $\gamma$ rays.

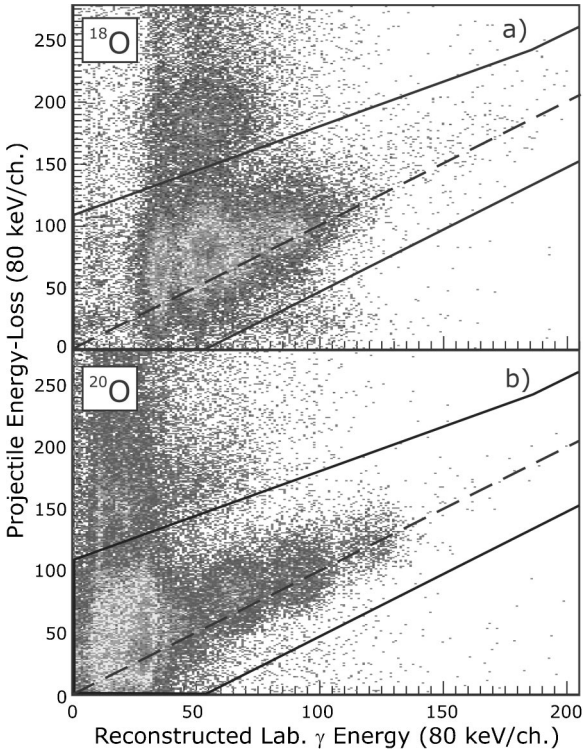


FIG. 3. Final event selection for the $^{18}O$ (a) and $^{20}O$ (b) studies. An energy-correlation gate is placed on a 2D histogram of projectile energy loss vs reconstructed, laboratory frame, $\gamma$-ray energy.

To improve the $BaF_2$ photopeak detection efficiency for individual photons, $\gamma$-ray hits in individual $BaF_2$ detectors, having been identified by the prescribed method, were processed event by event using a shower reconstruction routine that analyzed the hit patterns and energy distributions for multiplicity $>1$ events. The energy deposited simultaneously into neighboring detectors was summed. The segmentation of the array allowed for an approximate determination of the $\gamma$-ray emission angle with respect to the recoiled projectile, which facilitated Doppler correction for individual $\gamma$-ray energies. This correction was necessary given that the velocity of the excited fragments was $0.43c$ in the laboratory frame.

Final event selection for these experiments involved the application of simultaneous energy constraints on S800 and $BaF_2$ information. Specifically, it was required that projectile energy loss be well correlated with total reconstructed, laboratory frame, $\gamma$-ray energy. Figure 3 shows data from both reactions. Notice the enhancement of events appearing along the diagonal (dashed line), which represents events where projectile energy loss is completely recovered as $\gamma$-ray energy. This final energy constraint was inclusive of events falling above and left of the diagonal, which resulted, for example, from cascade decays whereby the projectile's deexcitation process proceeded through an intermediate state and

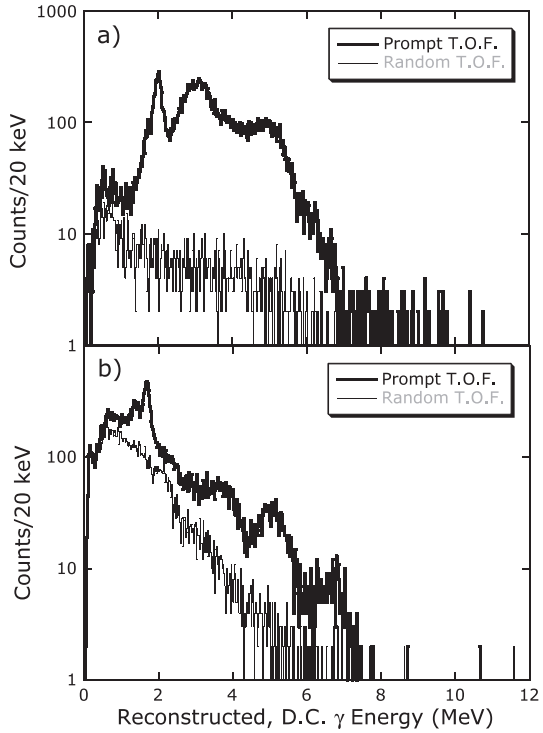


FIG. 4. Projection of both prompt and random TOF-gated events included within the S800-$BaF_2$ energy-correlation gates (shown in Fig. 3) onto the Doppler-corrected axis for $^{18}$O (a) and $^{20}$O (b). A subtraction yields the final $\gamma$-ray spectra.

one (or more) of the resulting $\gamma$-rays was not detected. The experimental energy resolution did not allow for the separation of these components. The resulting $BaF_2$ total-energy, $\gamma$-ray spectra for $^{18}$O and $^{20}$O are given in Figs. 4(a) and 4(b), respectively (thick black curves). Pronounced peaks observed at 2 MeV for $^{18}$O, and 1.7 MeV for $^{20}$O, correspond well with known $2_1^+$ energies (1.98 and 1.67 MeV), providing experimental verification of correct fragment identification and of the Doppler correction process. Figure 4 also shows the background contributions (thin gray lines) for each $\gamma$-ray energy spectrum. They were generated by simply shifting $\gamma$-ray TOF gates [e.g., Fig. 2(a)] by an rf period, thereby sampling the random contributions that were superimposed with the prompt $\gamma$-ray events. The same shower reconstruction analysis was performed on these random events; likewise the same S800-$BaF_2$ energy-correlation requirement was used as a final constraint. The final experimental $\gamma$-ray spectra were derived following a subtraction of these respective background distributions from the prompt $\gamma$ gated energy spectra.

## III. EXPERIMENTAL RESULTS

### A. The Monte Carlo simulation

To facilitate the correct interpretation of the experimental results and ultimately extract quantitative information, a Monte Carlo simulation was developed. Simulated $\gamma$-ray spectra were compared directly with those from experiment. The simulation made use of the intermediate energy Coulomb excitation formalism of Ref. [26], described in Sec. I B, to incorporate the inelastic excitation processes which occurred in both the projectile and the target. This treatment was sufficient since inelastic nuclear processes were negligible, given the small angular acceptance for these experiments ($\sim 1°$ in the laboratory frame).

Event by event, the inelastic excitation channel for the projectile (or target) was chosen based on the total integrated Coulomb excitation cross section $\sigma_n$ for each of the possible $n$ states (where $n$ is inclusive of target excited states). The $\sigma_n$ were calculated during the initialization sequence of the code after specifying the maximum laboratory-frame angular cone into which the projectiles could scatter. This cone was chosen to be much larger than the experimental acceptance (by a factor of $>2$). Having specified the excitation channel, the center-of-mass scattering angle for the projectile $\vartheta$ was chosen using the so-called Monte Carlo rejection method. This required knowledge of the $n$ Coulomb excitation angular distributions $d\sigma_n/d\vartheta$ which were calculated from expressions for the associated differential Coulomb excitation cross section expressions $d\sigma_n/d\Omega$ [equivalent to those presented in Eq. (5)]:

$$\frac{d\sigma}{d\vartheta} = 2\pi \sin\vartheta \frac{d\sigma}{d\Omega}. \tag{8}$$

The rejection method is as follows: two random numbers are generated. The first represents the abscissa, $x_{ran}$, which falls somewhere in the domain, $x_{min} \leqslant x_{ran} \leqslant x_{max}$, over which the probability function being generated, $P(x)$ [in this case, the differential cross section given above in Eq. (8)], is defined. The second random number $y_{ran}$ takes on values between 0 and $y_{max}$, where $y_{max}$ is the maximum value of the probability function over its limits. A simple comparison of $y_{ran}$ against $P(x_{ran})$ follows; the event, characterized by the physical observable $x_{ran}$, is generated if and only if $y_{ran} \leqslant P(x_{ran})$.

Computational efficiency was improved by simplifying the calculations of the center-of-mass Coulomb excitation angular distributions [Eq. (8)]. They were evaluated upon initialization only for discrete values of $\vartheta$, in steps of 0.1 mrad. Specifically, for any given stepwise angle $\vartheta_i$ the Coulomb excitation angular distribution was calculated by

$$\frac{d\sigma_{\pi\lambda,n}}{d\vartheta_i} = C(\pi\lambda,n)B(\pi\lambda,\text{g.s.}\rightarrow n)F[\vartheta_i,\xi(n),\pi\lambda], \tag{9}$$

where the quantities $F$, defined as

$$F[\vartheta_i,\xi(n),\pi\lambda] = \sin\vartheta_i \frac{df_{\pi\lambda}[\vartheta_i,\xi(n)]}{d\Omega_i}, \tag{10}$$

had been tabulated beforehand for each excitation channel using MATHEMATICA [47] and included into the simulation as input files. Explicit forms for the differential cross section functions $df_{\pi\lambda}/d\Omega$ appearing in Eq. (10), can be found, for example, in Refs. [26,27]. A direct comparison with Eq. (1) provides the definition for the constants:

$$C(E\lambda,n)=2\pi\left(\frac{Z_B\alpha}{\beta}\right)^2 a(n)^{-2\lambda+2},$$

$$C(M\lambda,n)=2\pi(Z_B\alpha)^2 a(n)^{-2\lambda+2}. \quad (11)$$

For target excitations $Z_B$ has to be replaced with $Z_A$ in the above expressions. Because the rejection method required knowledge of the Coulex angular distributions for any randomly chosen value of $\vartheta$ on an event-by-event basis, a cubic spline interpolation (e.g., Ref. [48]) was utilized to approximately convert the Coulomb excitation angular distributions to continuous functions.

Following excitation, only $\gamma$-ray decay was considered for projectile or target deexcitation since no excitations above the particle thresholds were included. The deexcitation paths were chosen based on the relevant $\gamma$ branching. The process of projectile $\gamma$-ray emission necessarily remained consistent with full momentum conservation for the excited-projectile/$\gamma$-ray system. (The inclusion of projectile recoil was critical for a good reproduction of the experimental S800 information.) For target $\gamma$ decay, the target nucleus was assumed stationary.

The $\gamma$-ray analysis relied on the radiation detection code GEANT (version 3.21) [49]. The total energy deposition information provided by GEANT was folded with the experimental $BaF_2$ energy resolution, characterized by the full width at half maximum (FWHM) $\Delta_{FWHM}$ for each simulated detector, event by event. The width was approximated by the functional dependence:

$$\Delta_{FWHM}(E_\gamma)\simeq E_\gamma\left(A+\frac{B}{\sqrt{E_\gamma}}\right). \quad (12)$$

$E_\gamma$ is the photopeak centroid energy of the detected $\gamma$ ray, while $A$ and $B$ are constants that were determined from a three-point fit of the experimental widths for calibration data. Energies of 898, 1836, and 4438 keV from two different radioactive sources, namely, $^{88}$Y and PuBe, were used for this calibration. The simulated $BaF_2$ information was filtered through the same analysis code that was used for the experimental $BaF_2$ data.

Another consideration for the simulation with regard to $\gamma$-ray response was the application of energy threshold constraints to these simulated $BaF_2$ signals. During the experiment, only those events where at least one detector recorded a fast-light signal larger than $T_h$ (the high threshold) were accepted by the computer acquisition. Additionally, for any given detector within a valid event, charge integration only occurred for fast signals larger than $T_l$, the low threshold. The threshold effects were included into the simulation by setting a unique set of threshold values for each detector during the initialization sequence, such that the average of these threshold values over all detectors were free parameters, $T_l^{Ave}$ and $T_h^{Ave}$, which were adjusted upon comparison with experimental data.

Figure 5 shows the good agreement of the simulated calibration data (solid lines) with the experimental equivalent for both $^{88}$Y and PuBe. The data acquisition for these calibration runs was operated in a mode whereby $T_h^{Ave}$ was equal to $T_l^{Ave}$; therefore the comparison of these data against these simulated curves could be used to determine the average low threshold setting ($T_l^{Ave}=650$ keV) for later $^{18,20}$O simulations.

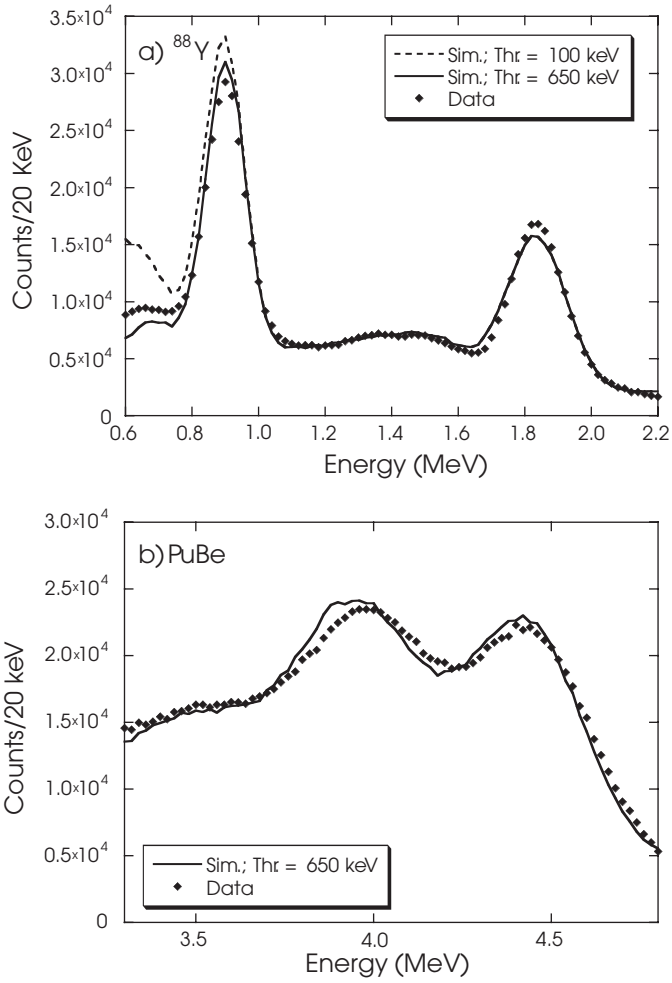


FIG. 5. Comparison of simulated (lines) and experimental (points) $BaF_2$ calibration data for $^{88}$Y (a) and PuBe (b). A linear background has been included in the simulated spectra. Good overall agreement is established using the simulated data with threshold settings of 650 keV (see text).

The GEANT simulation could be used to calculate the photopeak detection efficiency shown in Fig. 6. Shower reconstruction was enabled and events recording energies within $\pm 2\sigma$ of the emitted $\gamma$-ray energy were counted. The high thresholds were lowered to $T_h^{Ave}=T_l^{Ave}=500$ keV to minimize their bias on the shape at low $\gamma$-ray energies.

In general, a simplified approach was followed to account for the S800 response within the simulation. Experimentally, the energy and angular spreading of the observed projectiles was due to intrinsic dispersion in the beam, energy, and angular straggling in the $^{208}$Pb target and the finite resolving power of the S800 focal plane detectors. For the simulation, it was adequate to assume that the incoming projectiles were monoenergetic and then account for these energy-smearing effects by modifying the outgoing (after target) projectile

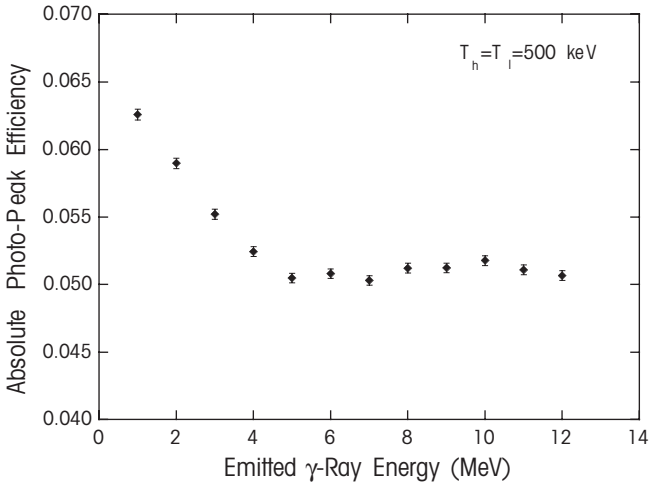


FIG. 6. $BaF_2$ photopeak efficiency ($\pm 2\sigma$; with shower reconstruction) for $\gamma$ rays emitted isotropically from a stationary source at the target position as computed by the GEANT simulation. The error bars included are purely statistical. The high thresholds were lowered to $T_h^{\mathrm{Ave}}=T_l^{\mathrm{Ave}}=500$ keV, so as to minimize their bias on the shape at low $\gamma$-ray energies.

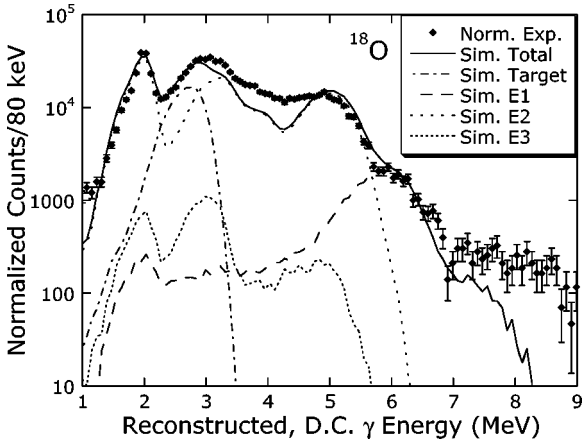


FIG. 7. Final $^{18}$O experimental $\gamma$-ray spectrum (diamonds) shown with the result from the simulation (solid line). The absolute normalization is arbitrary. The error bars included with the experimental data are purely statistical. The individual components that contribute to the simulated strength function, namely, projectile $E1$, $E2$, $E3$, and target background, are also shown. (Projectile $M2$ contributions are off-scale, as displayed.)

energies accordingly. The intrinsic beam angular dispersion and angular straggling in the target was folded into the incoming projectile trajectories. Simulated events were then constrained beyond the target by placing a free-form 2D cut in $(\theta,\phi)$ (dispersive and nondispersive scattering angles), which was similar to the shape of the analogous 2D experimental scattering distribution. Additional angular spreading due to the finite S800 detector resolution was then introduced for those simulated projectiles that scattered within this 2D acceptance window.

An additional consideration for the simulation was the presence of a beam blocker that was placed just upstream of the S800 focus to prevent an elastically scattered beam from overwhelming the particles that scattered inelastically. The incorporation of the blocker into the simulation was vital, as the low-energy portion of the inelastic distribution was unavoidably affected by its presence. Indeed, the blocker's influence on S800 angular acceptance was, effectively, incorporated into the simulation following the treatment described immediately above, rather by design. To include its effects with regard to projectile kinetic energy, only those projectiles having an energy-loss $\Delta E_p$ greater than $E_{\mathrm{Blkr}}$ were accepted for further analysis, i.e.,

$$\Delta E_p = E_{p,lab} - E'_{p,lab} \geqslant E_{\mathrm{Blkr}}, \tag{13}$$

where $E_{p,lab}$ and $E'_{p,lab}$ refer to the projectile's kinetic energy in the laboratory frame before and after the interaction with the target. $E_{\mathrm{Blkr}}$ was treated as a quasifree parameter for $^{18,20}$O simulations, as its value could not be determined experimentally with high precision ($\sim$500 keV).

### B. $^{18}$O results

Figure 7 shows the final experimental $^{18}$O strength distribution (diamonds) on a logarithmic scale. The spectrum is dominated at low energies by the excitation and decay of the first-excited $2^+$ state at 1.98 MeV. The broad peak near 3 MeV is primarily a convolution of two components, namely, decays of the $2_3^+$ state, which have proceeded through the $2_1^+$ level, and deexcitations from the $2_1^+$ level in $^{208}$Pb at 4.09 MeV (the later contributions have been shifted to 2.7 MeV following the Doppler correction). The peak near 5 MeV results from ground-state decays of the $2_3^+$ level.

These assignments were deduced from the simulation, the results of which are shown as the solid line in Fig. 7. (The experimental results have been normalized arbitrarily to the simulated data in the region between 2.3 and 2.9 MeV.) The simulation was generated following the incorporation of the known $^{18}$O and $^{208}$Pb level schemes and the associated $B(\pi\lambda)$ information (see Table II) as well as the known $\gamma$-ray decay-branching ratios, given in Table VI. The two free parameters for the simulation, namely, the average high threshold setting $T_h^{\mathrm{Ave}}$ and the blocker (energy) position $E_{\mathrm{Blkr.}}$ were adjusted to 3.1 and 3.3 MeV, respectively, to produce the best overall agreement with the experimental results.

Figure 7 also includes the individual components (projectile $E1$,$E2$,$E3$, and target background) which contribute to the total simulated strength function. Not surprisingly, projectile $M2$ excitations are strongly suppressed relative to the other excitation channels; they appear below the displayed $y$ scale. The figure demonstrates that projectile $E2$ excitations (dot-spaced curve) dominate the overall $^{18}$O $\gamma$-ray spectrum. Essentially, $E1$ excitations (dashed curve) contribute only above approximately 5.7 MeV. The shoulder appearing in the experimental curve near 6 MeV is the result of excitations to the $1_2^-$ at 6.20 MeV. It is also evident that target excitations are important. In the region between approximately 2.2 and 2.9 MeV, target excitations (dot-dashed curve) are, in fact, the dominant contribution.

Overall, the result from the simulation describes the experimental data well, with the exception of the region be-

TABLE VI. Known branching ratios [31] used to generate the $^{18}$O simulated results presented in Fig. 7. The $2_1^+$ and $3_1^-$ levels in the target that decay directly to the ground state with 100% probability are not included.

| $E_i$ (MeV) | $J^\pi_{n,i}$ | $E_f$ (MeV) | $J^\pi_{n,f}$ | $E_\gamma$ (MeV) | Branching ratio (%) |
|---|---|---|---|---|---|
| 1.98 | $2_1^+$ | 0.00 | $0_1^+$ | 1.98 | 100 |
| 3.55 | $4_1^+$ | 1.98 | $2_1^+$ | 1.57 | 100 |
| 3.63 | $0_2^+$ | 1.98 | $2_1^+$ | 1.65 | 99.7 |
| | | 0.00 | $0_1^+$ | 3.63 | 00.3 |
| 3.92 | $2_2^+$ | 1.98 | $2_1^+$ | 1.94 | 87.6 |
| | | 0.00 | $0_1^+$ | 3.92 | 12.4 |
| 4.46 | $1_1^-$ | 3.92 | $2_2^+$ | 0.54 | 02.5 |
| | | 3.63 | $0_2^+$ | 0.83 | 70.4 |
| | | 1.98 | $2_1^+$ | 2.48 | 27.1 |
| 5.10 | $3_1^-$ | 3.92 | $2_2^+$ | 1.18 | 17.6 |
| | | 3.55 | $4_1^+$ | 1.55 | 06.3 |
| | | 1.98 | $2_1^+$ | 3.12 | 76.1 |
| 5.26 | $2_3^+$ | 4.46 | $1_1^-$ | 0.80 | 03.0 |
| | | 3.92 | $2_2^+$ | 1.34 | 08.7 |
| | | 3.63 | $0_2^+$ | 1.63 | 01.0 |
| | | 3.55 | $4_1^+$ | 1.71 | 01.1 |
| | | 1.98 | $2_1^+$ | 3.28 | 55.9 |
| | | 0.00 | $0_1^+$ | 5.26 | 30.3 |
| 5.34 | $0_3^+$ | 4.46 | $1_1^-$ | 0.88 | 42.0 |
| | | 1.98 | $2_1^+$ | 3.36 | 58.0 |
| 5.53 | $2_1^-$ | 4.46 | $1_1^-$ | 1.07 | 27.0 |
| | | 3.92 | $2_2^+$ | 1.61 | 24.0 |
| | | 1.98 | $2_1^+$ | 3.55 | 49.0 |
| 6.20 | $1_2^-$ | 5.34 | $0_3^+$ | 0.86 | 01.1 |
| | | 5.26 | $2_3^+$ | 0.94 | 03.6 |
| | | 4.46 | $1_1^-$ | 1.74 | 04.1 |
| | | 3.63 | $0_2^+$ | 2.57 | 02.5 |
| | | 0.00 | $0_1^+$ | 6.20 | 88.7 |
| 6.35 | $2_2^-$ | 4.46 | $1_1^-$ | 1.89 | 13.0[a] |
| | | 3.92 | $2_2^+$ | 2.43 | 55.0 |
| | | 1.98 | $2_1^+$ | 4.37 | 32.0 |
| 6.40 | $3_2^-$ | 5.26 | $2_3^+$ | 1.14 | 05.6 |
| | | 5.10 | $3_1^-$ | 1.30 | 09.8 |
| | | 4.46 | $1_1^-$ | 1.94 | 02.8 |
| | | 3.92 | $2_2^+$ | 2.48 | 06.3 |
| | | 3.55 | $4_1^+$ | 2.85 | 07.4 |
| | | 1.98 | $2_1^+$ | 4.42 | 68.1 |
| 7.62 | $1_3^-$ | 6.20 | $1_2^-$ | 1.42 | 01.0 |
| | | 5.34 | $0_3^+$ | 2.28 | 06.0 |
| | | 4.46 | $1_1^-$ | 3.16 | 08.0 |
| | | 1.98 | $2_1^+$ | 5.64 | 62.0 |
| | | 0.00 | $0_1^+$ | 7.62 | 23.0 |
| 7.77 | $2_3^-$ | 5.10 | $3_1^-$ | 2.67 | 36.0 |
| | | 4.46 | $1_1^-$ | 3.31 | 11.0 |
| | | 1.98 | $2_1^+$ | 5.79 | 53.0 |

[a]Adjusted within reported uncertainty.

tween 3 and 4.5 MeV, where it fails to account for the full intensity in the measured spectrum. The cause for the discrepancy is not fully understood.

Nevertheless, the conclusion that projectile $E2$ excitations dominate the observed $^{18}$O $\gamma$-ray spectrum is clearly justified. Target excitations, especially contributions from the $2_1^+$ state, play an important role. In short, one can conclude from the $^{18}$O comparison that the simulation has successfully reproduced the important features of the observed $\gamma$-ray spectrum, and hence, its extension to the less-known case of $^{20}$O is credible.

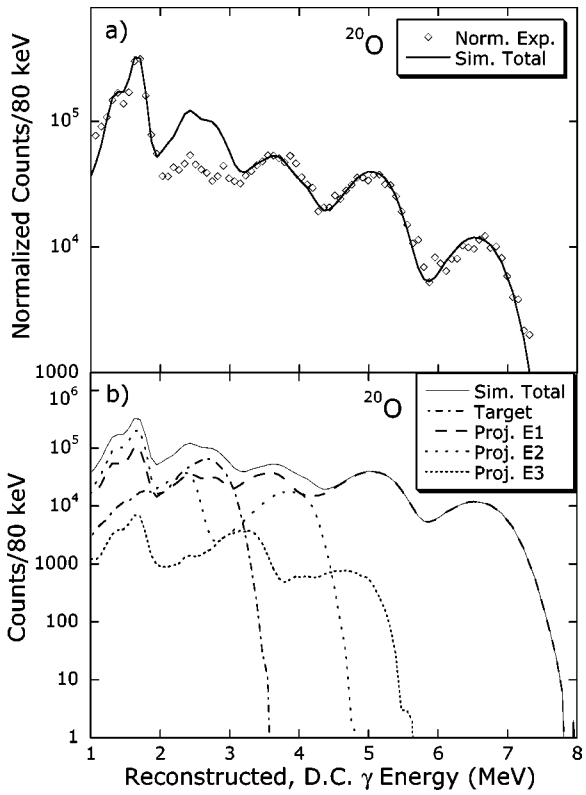


FIG. 8. (a) Results from a preliminary $^{20}$O simulation (solid line) shown with the experimental strength distribution (open diamonds). The strength observed between approximately 2 and 3 MeV is not reproduced, which indicates the need for a boosting of the input $B(E1)$ transition probabilities (see text). (b) The individual components ($E1$, $E2$, $E3$, and target) that contribute to the overall simulated strength function. The projectile-$E1$ strength dominates the spectrum. Specifically, the structures above 3 MeV are mainly the result of excitations to two $1^-$ states that are found to exist at 5.35 and 6.85 MeV.

### C. $^{20}$O results

The final $^{20}$O $\gamma$-ray spectrum is displayed logarithmically by the open diamonds in Fig. 8(a). Again, a dominant feature is the excitation and decay of the projectile $2_1^+$ state at 1.67 MeV. The lowest-energy peak at 1.35 MeV is primarily an escape peak for the 1.67-MeV photopeak. (This structure is visible for $^{20}$O and not for $^{18}$O because the high energy thresholds were significantly reduced in the $^{20}$O case.) As before, target contributions play a role near 2.7 MeV. The small but noticeable peak at slightly lower excitation energy (approximately 2.4 MeV) is likely a convolution where contributions include $2_2^+ \rightarrow 2_1^+$ decays. At higher excitation energies, approaching the neutron binding energy (7.608 MeV), two peaks are clearly visible at approximately 5.2 and 6.6 MeV. These peaks could already be seen in the 2D plot of Fig. 3(b) as the two highest-energy enhancements on the

TABLE VII. $^{20}$O and $^{208}$Pb level schemes utilized in the production of the simulated results presented in Figs. 8 and 9. In order to fit the observed $\gamma$-ray spectra, two previously unobserved $1^-$ levels have been included. The state included at 5.00 MeV does not have confirmed spin and parity, rather it has been simply assigned as $3^-$ for demonstrative purposes since theoretical calculations [36] predict a $3^-$ level at 5 MeV (see Table III). The values in square brackets indicate power of 10.

| Incorporated level schemes | | | Fig. 8 | Fig. 9 |
|---|---|---|---|---|
| | $E_x$ (MeV) | $J^\pi$ | $B(E\lambda)\uparrow$ ($e^2$ fm$^{2\lambda}$) | |
| $^{20}$O | 1.67 | $2^+$ | 2.80 [+01] | 3.00 [+01] [a] |
| | 4.07 | $2^+$ | 9.00 [+00] | 3.00 [+01] |
| | 5.00 | $3^-$ | 1.60 [+03] | 1.60 [+03] |
| | 5.23 | $2^+$ | 7.00 [-04] | 7.00 [-04] |
| | 5.35 | $1^-$ | 1.35 [-02] | 6.20 [-02] |
| | 6.85 | $1^-$ | 1.10 [-02] | 3.50 [-02] |
| $^{208}$Pb | 2.61 | $3^-$ | 6.11 [+05] | 6.11 [+05] |
| | 4.09 | $2^+$ | 2.60 [+03] [b] | 2.60 [+03] [b] |

[a]Increased within the known uncertainty [33].
[b]Reduced within the known uncertainty [34].

diagonal, which is an indication that these excited $^{20}$O configurations have strong direct ground-state decay branches.

The above interpretations have been, in part, deduced by comparison with simulation. A preliminary comparison of the final $^{20}$O experimental $\gamma$-ray spectrum with a simulated equivalent (solid line) is presented in Fig. 8(a). For these simulated results, $T_h^{\mathrm{Ave}}$ and $E_{\mathrm{Blkr}}$ were set to 1.45 and 2.52 MeV, respectively. The experimental result has been normalized, again arbitrarily, to the simulated data in the region between 4.5 and 8 MeV. Above the region of 3 MeV the simulated and experimental line shapes are in good agreement. To facilitate this, two previously unobserved excited $1^-$ states were incorporated at 5.35 and 6.85 MeV.

The arguments for assigning these states as $1^-$ rather than $2^+$ are twofold. First, strong direct ground-state branches were observed for these states, which is more consistent with a dipole character. Second, as was discussed in Sec. I C, shell-model calculations for $^{20}$O predict that the $B(E2)$ strengths for the $2^+_{2,3,4}$ states will be reduced (especially for the highest $2^+_4$ state) as compared to $^{18}$O, whereas the opposite is true for the predicted $1^-$ states. Following the inclusion of these two $1^-$ levels, $E1$ strength is shown to be the dominant contribution to the overall $\gamma$-ray spectrum, as evidenced by the individual components in Fig. 8(b).

Table VII lists all the excitation parameters for the preliminary $^{20}$O simulation presented in Fig. 8. The $B(E1)$ transition strengths for the 5.35 and 6.85 MeV states were adjusted to $0.0135e^2$ fm$^2$ and $0.0110e^2$ fm$^2$, respectively. As can be verified with a comparison with Table III, these strengths are significantly higher than the WBP shell-model calculations predict for $1^-$ levels in this region. For example, the preliminary $B(E1)$ for the lower energy state at 5.35 MeV is factors of 6 and 8 larger than that for predicted $1^-$ levels at 5.1 and 6.2 MeV, respectively.

Target excitations provide crucial evidence that the $B(E1)$ strengths for these $1^-$ levels are in fact larger still.

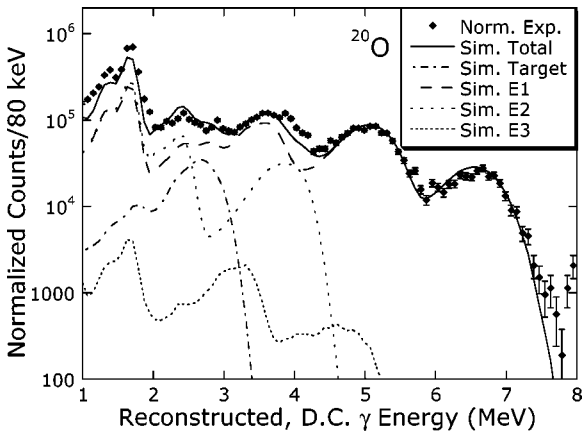


FIG. 9. Results of the final $^{20}$O simulation (solid line) presented against the experimental $\gamma$-ray spectrum (diamonds). The error bars included with the experimental data are purely statistical. The agreement between 2 and 3 MeV has improved significantly. The individual components ($E1$, $E2$, $E3$, and target) that contribute to the total simulated $\gamma$-ray spectrum are also included.

The preliminary simulation overproduces $\gamma$-ray intensity between 2 and 3 MeV. As demonstrated by the different contributions presented in Fig. 8(b), this is the region where $\gamma$ rays from the first-excited $2^+$ state in the target and the $2^+_2 \rightarrow 2^+_1$ decays in the projectile are the dominant contributions. The only way to improve the agreement between 2 and 3 MeV is to simultaneously increase the $B(E1)$ values for the $1^-$ projectile levels while decreasing their $2^+_2$ decay branching, effectively reducing the relative intensity of the discrepancy (by boosting the $\gamma$-ray intensities below and above).

TABLE VIII. $^{20}$O branching scheme used for the simulated results presented in Fig. 9. Only the branching from the $2^+_2$ state has been previously established [21].

| $E_i$ (MeV) | $J^\pi_{n,i}$ | $E_f$ (MeV) | $J^\pi_{n,f}$ | $E_\gamma$ (MeV) | Branching ratio (%) |
|---|---|---|---|---|---|
| 1.67 | $2^+_1$ | 0.00 | $0^+_1$ | 1.67 | 100 |
| 3.57 [a] | $4^+_1$ | 1.67 | $2^+_1$ | 1.90 | 100 |
| 4.07 | $2^+_2$ | 1.67 | $2^+_1$ | 2.40 | 74 |
| | | 0.00 | $0^+_1$ | 4.07 | 26 |
| 4.46 [a] | $0^+_2$ | 1.67 | $2^+_1$ | 2.79 | 100 |
| 5.00 | $3^-_1$ | 4.07 | $2^+_2$ | 0.93 | 18 |
| | | 3.57 | $4^+_1$ | 1.43 | 6 |
| | | 1.67 | $2^+_1$ | 3.33 | 76 |
| 5.23 | $2^+_3$ | 4.07 | $2^+_2$ | 1.16 | 10 |
| | | 1.67 | $2^+_1$ | 3.56 | 60 |
| | | 0.00 | $0^+_1$ | 5.23 | 30 |
| 5.35 | $1^-_1$ | 4.46 | $0^+_2$ | 0.89 | 19 |
| | | 4.07 | $2^+_2$ | 1.28 | 5 |
| | | 1.67 | $2^+_1$ | 3.68 | 46 |
| | | 0.00 | $0^+_1$ | 5.35 | 30 |
| 6.85 | $1^-_2$ | 4.07 | $2^+_2$ | 2.78 | 10 |
| | | 1.67 | $2^+_1$ | 5.18 | 39 |
| | | 0.00 | $0^+_1$ | 6.85 | 51 |

[a]Known energy and spin-parity from Ref. [21].

TABLE IX. Summary of the extracted $^{20}$O results compared with three sets of shell-model calculations. The values in square brackets indicate powers of 10.

| Expt. results | | | WBP [a] | | | WB10 [b] | | | WB10 ($p$-$sd$ gap reduction) [c] | | |
|---|---|---|---|---|---|---|---|---|---|---|---|
| $J^\pi$ | $E_x$ (MeV) | $B(E1)\uparrow$ [d] | $J_n^\pi$ | $E_x$ (MeV) | $B(E1)\uparrow$ | $J_n^\pi$ | $E_x$ (MeV) | $B(E1)\uparrow$ | $J_n^\pi$ | $E_x$ (MeV) | $B(E1)\uparrow$ |
| | | | | | | | | | $1_1^-$ | 4.10 | 3.7 [-04] |
| $1^-$ | 5.35(10) | 6.2(16) [-02] | $1_1^-$ | 5.05 | 2.4 [-03] | $1_1^-$ | 5.34 | 2.3 [-03] | $1_2^-$ | 5.47 | 2.5 [-03] |
| | | | $1_2^-$ | 6.16 | 1.7 [-03] | $1_2^-$ | 6.55 | 1.7 [-03] | $1_3^-$ | 6.06 | 8.9 [-03] |
| $1^-$ | 6.85(5) | 3.5(9) [-02] | $1_3^-$ | 7.24 | 1.4 [-03] | $1_3^-$ | 7.20 | 7.6 [-03] | $1_4^-$ | 6.75 | 1.4 [-02] |
| | | | $1_4^-$ | 7.74 | 4.1 [-02] | $1_4^-$ | 7.89 | 1.8 [-02] | $1_5^-$ | 7.45 | 2.4 [-02] |
| EWS[Expt.]: 0.57(11) [e] | | | EWS[$1_1^- \rightarrow 1_3^-$]: 0.033 | | | EWS[$1_1^- \rightarrow 1_3^-$]: 0.078 | | | EWS[$1_2^- \rightarrow 1_4^-$]: 0.16 | | |

[a]References [38,36].
[b]References [38,50].
[c]References [1,38,50].
[d] $[B(E1)] = e^2\text{fm}^2$.
[e] $[\text{EWS}] = e^2\text{fm}^2$ MeV.

Figure 9 presents the final fit to the experimental results. The parameters $T_h^{\text{Ave}}$ and $E_{\text{Blkr}}$ were adjusted to 1.0 and 1.8 MeV, respectively. (Again, the normalization region is 4.5 to 8 MeV.) The excitation parameters for this final comparison are also included in Table VII. The $B(E1)$ strengths for the $1^-$ states have been increased substantially. For example, the 5.35 MeV state is found to have a $B(E1)\uparrow$ strength of $\simeq 0.062e^2$ fm$^2$, which is a factor of 26 and 36 larger than the predicted WBP states at 5.1 and 6.2 MeV, respectively (compare with Table III). Meanwhile, the $B(E1)\uparrow$ strength of the higher energy $1^-$ state is $\simeq 0.035e^2$ fm$^2$, which is 20 and 25 times larger than the transition strengths for the closest predicted WBP levels at 6.2 and 7.2 MeV, respectively.

The detailed $^{20}$O $\gamma$-decay branching ratios which were incorporated into the final $^{20}$O simulation are given in Table VIII. As previously indicated, only the branching ratios for the $2_2^+$ state are known [21]. The branching probabilities used for the incorporated $0_2^+$, $3_1^-$, and $2_3^+$ states were taken from $^{18,20}$O systematics. These levels do not play an important role in the strength distribution, so that it is not possible to extract any quantitative information for these states. The estimated uncertainty in the branching ratios for the $1^-$ states is $\pm 20$. This estimate was taken from comparisons of the $1^-$ branching used for the final fit and for the preliminary $^{20}$O simulations.

A reasonable estimate for the extracted transition strengths for the new $1^-$ levels at 5.35 and 6.85 MeV could be deduced. A $\chi^2$ analysis was performed that involved scaling the input $B(E1)$ values for these states together while keeping their decay branching ratios fixed. Similar agreement between the $^{20}$O simulation and the experimental result was obtained up to a transition probability scaling of $\pm 25\%$. Hence, we extract transition strengths of $0.062(16)e^2$ fm$^2$ and $0.035(9)e^2$ fm$^2$ for the states at 5.35 and 6.85 MeV, respectively.

## IV. DISCUSSION

Table IX summarizes the present results for comparison with three sets of shell-model calculations for discrete $1^-$ states in $^{20}$O. The WBP calculations included are identical with those presented in Table III, while the two remaining sets of calculations are the result of employing the complementary $0s0p$-$1s0d$-$1p0f$-WB10 (or WBT) residual interaction [38]. As indicated, the second set of WB10 calculations has incorporated a 1.31-MeV $p$-$sd$ shell-gap reduction [1,50].

While the 5.35(10) MeV state can likely be associated with a specific calculated state, it is not possible to uniquely assign the 6.85(5) MeV state with one calculated level. However, the estimated energy uncertainty of the calculations is approximately 500 keV and all sets of theoretical calculations agree with the data within this uncertainty. Hence, for comparison of the extracted transition strengths with theory, an energy-weighted sum (EWS) has been computed for the three levels that are within 500 keV of the 5.35 and 6.85 MeV experimental states.

As mentioned in Sec. III C, the transition strengths of the observed $1^-$ states were necessarily increased above the WBP calculated values which provided the initial guidance. The sensitivity of the discrete $1^-$ levels to the parametrization of the residual interaction used in the shell-model calculations is demonstrated by the EWS increase comparing the WBP result versus that for the unmodified set of WB10 calculations. The incorporation of a $p$-$sd$ shell-gap reduction into the WB10 calculations results in a gain in EWS strength. The fact that these calculations agree better with experiment likely reveals weaker valence-neutron binding as the mechanism for low-lying dipole strength.

The main difference between the $^{18}$O and $^{20}$O $\gamma$-ray spectra is the marked onset of $E1$ strength in $^{20}$O. A comparison of the transition strengths in Table I with those incorporated into the $^{20}$O simulation (Table VII) reveals that while $E2$ strength is slightly suppressed in $^{20}$O relative to $^{18}$O, the newly observed $1^-$ states dominate not only the region above 5 MeV but nearly the entire $^{20}$O spectrum. It is also interesting to compare the present Coulomb excitation data with the in-beam $\gamma$ spectrum of $^{20}$O following the fragmentation of $^{36}$S at GANIL [23]. Figure 10 shows the $BaF_2$ $\gamma$-ray spectrum superimposed with the present data. Although the resolution is not as good in the in-beam case, similarities between the two datasets are apparent. A structure near 5 MeV agrees well with our identified $1^-$ state at 5.35 MeV. However, since the fragmentation reaction is not highly selective with respect to the spin parity of the popu-

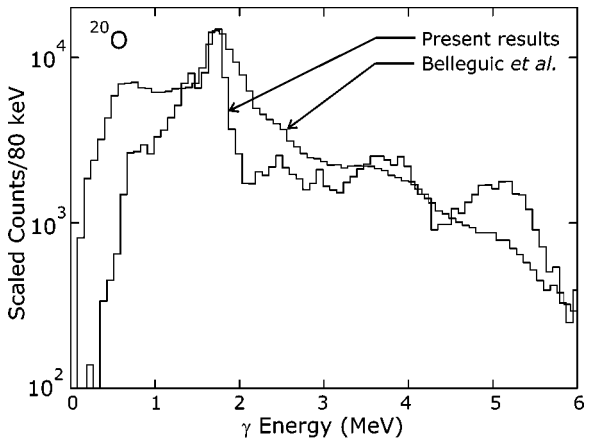


FIG. 10. Comparison of the present $^{20}$O results with a $BaF_2$ $\gamma$-ray spectrum reported following a recent in-beam $\gamma$-ray spectroscopy study [23]. Although similar structures are observed in the in-beam experiment, they may instead result from the population of the known $2^+$ states at 5.23 and 5.30 MeV.

lated levels, this enhancement may also result from excitation of the known $2^+$ states at 5.23 and 5.3 MeV [21]. In addition, the low-energy portion of the broad peak they observed near 3.7 MeV is likely due to the decay of these aforementioned states through the first-excited state.

The shell-model calculations in Table IX provide also a bridge between the current results and those following the virtual photon absorption experiment at GSI [19]. The sharp feature observed in their measured $^{20}$O strength function just above the neutron removal threshold likely can be associated with the calculated $1^-$ state that appears in all cases between 7.5 and 7.9 MeV.

Finally, we shall close the discussion with a comparison of the present results, in terms of summed transition strength (in Weisskopf units, W.u.) with some of the nuclei discussed in Sec. I as PDR candidates (see Table X). While the energy region included in these sums is not necessarily consistent, it is apparent that all PDR-candidate nuclei have a total, discrete-region $B(E1)$ strength of the order of $10^{-1}$ W.u. $^{20}$O exhibits a similarly large summed $B(E1)$ strength (via the two new states at 5.35 and 6.85 MeV), while this sum for $^{18}$O discrete dipole states is significantly lower.

While shell-model calculations give us some insight into the configuration of the wave functions for these $^{20}$O $1^-$ levels (see Table IV), the underlying cause for this strength remains unclear. Specifically, whether it can be attributed to a collective excitation of the skin, or rather, results from incoherent single-particle excitations is still an open question. Future experiments extending these studies further towards the neutron drip line are clearly necessary.

TABLE X. Summed $B(E1)$ strength for $^{18}$O, $^{20}$O, and heavier nuclei which are candidates for the presence of the PDR. The values in square brackets indicate powers of 10.

| Nuclide | $\Sigma B(E1)\uparrow$ (W.u.) | Energy region for sum (MeV) | Ref. |
|---|---|---|---|
| $^{18}$O | 6.35(86) [-3] | 6.0–8.0 | Present work, [29] |
| $^{20}$O | 2.0(5) [-1] | 5.0–7.0 | Present work |
| $^{48}$Ca | 6.54(48) [-2] | 5.0–10.0 | [7] |
| $^{116}$Sn | 1.33(16) [-1] [a] | 5.0–8.0 | [8] |
| $^{124}$Sn | 2.15(27) [-1] [a] | 5.0–8.0 | [8] |
| $^{138}$Ba | 1.55 [-1] [a,b] | 4.0–6.5 | [10] |
| $^{208}$Pb | 4.17(34) [-1] | 4.5–7.0 | [11] |

[a]Sum assumes unconfirmed parity of some levels is negative.
[b]Explicit sum not provided in reference.

## V. CONCLUDING REMARKS

In conclusion, we populated excited states in $^{18}$O and $^{20}$O by intermediate energy Coulomb excitation. Two new $1^-$ states in $^{20}$O were observed at 5.35(10) and 6.85(5) MeV in excitation energy. Their dipole character was established by shell-model predictions for states in this region and by the observation of strong direct ground-state decay branches among transitions from these levels. $B(E1)$ information has been extracted from comparison of the experimental results with those generated using a Monte Carlo simulation. The extracted transition strengths of $B(E1)\uparrow(5.35\ \mathrm{MeV}) \simeq 0.062(16)e^2\mathrm{fm}^2$ and $B(E1)\uparrow(6.85\ \mathrm{MeV}) \simeq 0.035(9)e^2\mathrm{fm}^2$ are significantly larger than predicted by the shell-model calculations, though their summed value is consistent with that for other nuclei that may exhibit the Pygmy dipole resonance. The agreement between the shell-model calculations and experiment can be improved by reducing the energy gap between the $p$ and $sd$ shells. This fact may demonstrate a simple mechanism for low-lying dipole strength in exotic nuclei. Still, within the context of collectivity, the underlying structure of the observed $1^-$ states needs to be clarified.

## ACKNOWLEDGMENTS

This work was supported by the National Science Foundation Grant No. PHY95-28844 and the Department of Energy under Grant No. DE-FG03-97ER41020/A000. Oak Ridge National Laboratory is managed by UT-Battelle, LLC, for the U.S. Department of Energy under Contract No. DE-AC05-00OR22725.

[1] H. Sagawa and T. Suzuki, Phys. Rev. C **59**, 3116 (1999).
[2] M. Matsuo, Nucl. Phys. **A696**, 371 (2001).
[3] T. Aumann *et al.*, Phys. Rev. C **59**, 1252 (1999).
[4] Y. Iwata *et al.*, Phys. Rev. C **62**, 064311 (2000).
[5] D. Sackett *et al.*, Phys. Rev. C **48**, 118 (1993).
[6] T. Nakamura *et al.*, Phys. Lett. B **331**, 296 (1994).
[7] T. Hartmann, J. Enders, P. Mohr, K. Vogt, S. Volz, and A. Zilges, Phys. Rev. C **65**, 034301 (2002).
[8] K. Govaert, F. Bauwens, J. Bryssinck, D.D. Frenne, E. Jacobs, W. Mondelaers, L. Govor, and V.Y. Ponomarev, Phys. Rev. C **57**, 2229 (1998).
[9] R.-D. Herzberg *et al.*, Phys. Lett. B **390**, 49 (1997).

[10] R.-D. Herzberg *et al.*, Phys. Rev. C **60**, 051307(R) (1999).
[11] J. Enders *et al.*, Phys. Lett. B **486**, 279 (2000).
[12] R. Mohan, M. Danos, and L.C. Beidenharn, Phys. Rev. C **3**, 1740 (1971).
[13] V. Soloviev, *Theory of Atomic Nuclei: Quasiparticles and Phonons* (Institute of Physics Publishing, Bristol, 1992).
[14] J. Chambers, E. Zaremba, J.P. Adams, and B. Castel, Phys. Rev. C **50**, R2671 (1994).
[15] J.P. Adams, B. Castel, and H. Sagawa, Phys. Rev. C **53**, 1016 (1996).
[16] N.D. Dang, V.K. Au, T. Suzuki, and A. Arima, Phys. Rev. C **63**, 044302 (2001).
[17] E. Tryggestad *et al.*, in *Low-Lying Dipole Strength in $^{20}$O, Proceedings of Frontiers of Nuclear Structure*, edited by P. Fallon and R. Clark, AIP Conf. Proc. No. 656 (AIP, Melville, NY, 2003), pp. 295–302.
[18] J.W. Jury, B.L. Berman, D.D. Faul, P. Meyer, and J.G. Woodworth, Phys. Rev. C **21**, 503 (1980).
[19] A. Leistenschneider *et al.*, Phys. Rev. Lett. **86**, 5442 (2001).
[20] R.L. Varner, N. Gan, J.R. Beene, M.L. Halbert, D.W. Stracener, A. Azhari, E. Ramakrishnan, P. Thirolf, M.R. Thoennessen, and S. Yokayama, in *ENAM98, Exotic Nuclei and Atomic Masses*, edited by Bradley M. Sherrill, David J. Morrissey, and Cary N. David, AIP Conf. Proc. 455 (AIP, Woodbury, NY, 1998).
[21] D.R. Tilley, C.M. Cheves, J.H. Kelley, S. Raman, and R.H. Weller, Nucl. Phys. **A636**, 249 (1998).
[22] E. Khan *et al.*, Phys. Lett. B **490**, 45 (2000).
[23] M. Belleguic *et al.*, Nucl. Phys. **A682**, 136c (2001).
[24] P.G. Thirolf *et al.*, Phys. Lett. B **485**, 16 (2000).
[25] E. Tryggestad *et al.*, Phys. Lett. B **541**, 52 (2002).
[26] K. Alder and A. Winther, *Electromagnetic Excitation: Theory of Coulomb Excitation with Heavy Ions*, 1st ed. (North-Holland, Amsterdam, 1975).
[27] K. Alder, A. Bohr, T. Huus, B. Mottelson, and A. Winther, Rev. Mod. Phys. **28**, 432 (1956).
[28] B.E. Norum *et al.*, Phys. Rev. C **25**, 1778 (1982).
[29] D.M. Manley *et al.*, Phys. Rev. C **43**, 2147 (1991).
[30] R.M. Sellers, D.M. Manley, M.M. Niboh, D.S. Weerasundara, R.A. Lindgren, B.L. Clausen, M. Farkhonheh, B.E. Norum, and B.L. Berman, Phys. Rev. C **51**, 1926 (1995).
[31] D.R. Tilley, H.R. Weller, C.M. Cheves, and R.M. Chasteler, Nucl. Phys. **A595**, 1 (1995).
[32] G. Arfken, *Mathematical Methods for Physicists*, 3rd ed. (Academic, New York, 1985).
[33] S. Raman, C.W. Nestor, Jr., S. Kahane, and K.H. Bhatt, At. Data Nucl. Data Tables **42**, 1 (1989).
[34] R.H. Spear, At. Data Nucl. Data Tables **42**, 55 (1989).
[35] M.J. Martin, Nucl. Data Sheets **47**, 797 (1986).
[36] B. A. Brown (private communication).
[37] B.A. Brown and B.H. Wildenthal, Annu. Rev. Nucl. Part. Sci. **38**, 29 (1988), the *sd*-shell energies obtained with the USD interaction can be found online at http://www.nscl.msu.edu/~brown/sde.htm.
[38] E.K. Warburton and B.A. Brown, Phys. Rev. C **46**, 923 (1992).
[39] R.L. Lawson, F.J.D. Serduke, and H.T. Fortune, Phys. Rev. C **14**, 1245 (1976).
[40] B.M. Sherrill, D.J. Morrissey, J.A. Nolen, Jr., N. Orr, and J.A. Winger, Nucl. Instrum. Methods Phys. Res. B **70**, 298 (1992).
[41] J. A. Caggiano, Ph.D. thesis, Michigan State University, 1999.
[42] J. Yurkon, D. Bazin, W. Benenson, D.J. Morrissey, B.M. Sherrill, D. Swan, and R. Swanson, Nucl. Instrum. Methods Phys. Res. A **422**, 291 (1999).
[43] N. P. Shaw, Ph.D. thesis, State University of New York at Stony Brook, 1999.
[44] E. Tryggestad, Ph.D. thesis, Michigan State University, 2001, this document is available online at http://www.nscl.msu.edu/~tryggest/pdf/thesis.pdf
[45] M. Laval, M. Moszyński, R. Allemand, E. Cormoreche, P. Guinet, R. Odru, and J. Vacher, Nucl. Instrum. Methods Phys. Res. **206**, 169 (1983).
[46] G. F. Knoll, *Radiation Detection and Measurement*, 3rd ed. (Wiley, New York, 2000).
[47] S. Wolfram, *The MATHEMATICA Book*, 4th ed. (Cambridge University Press, Cambridge, England, 1999).
[48] W. H. Press, S. A. Teukolsky, W. T. Vetterling, and B. P. Flannery, *Numerical Recipes in FORTRAN: the Art of Scientific Computing*, 2nd ed. (Cambridge University Press, Cambridge, England, 1992).
[49] GEANT—Detector Description and Simulation Tool, Application Software Group, Computing and Networks Division, CERN, Geneva, Switzerland, 1993.
[50] T. Suzuki (private communication).